



Full Length Article

Evaluation of the fracture energy of magnesium via ballistic impact experiments

M Burley, TW Clyne*

Department of Materials Science and Metallurgy, Cambridge University, 27 Charles Babbage Road, Cambridge CB3 0FS, UK



ARTICLE INFO

Keywords:

High strain rates
Ballistic impact indentation
Finite element analysis
Plasticity
Fracture energy
Strain energy release rates
X-ray tomography

ABSTRACT

This paper concerns experimental study and modeling of the ballistic impact (indentation) of spherical projectiles into thick metallic (Mg) samples, and resultant crack propagation characteristics. A previously-described procedure is first used to evaluate the Johnson–Cook parameter for the strain rate sensitivity of plastic deformation for this material ($C \sim 0.026$). The main emphasis, however, is on study of its fracture characteristics (under high imposed strain rates), with tomographic imaging being used to obtain crack patterns for different projectile velocities. It is recognized that there are many situations, including the one being studied here, for which use of a critical plastic strain criterion for prediction of fracture is inappropriate. An approach based on fracture mechanics, and on use of FEM modeling to estimate the strain energy release rate required for crack propagation (i.e. the fracture energy of the material) is proposed and applied to these experimental results, leading to a value of the order of 2 kJ m^{-2} . While such a procedure is unlikely to produce accurate values, partly because the crack propagation takes place under local conditions that change rapidly and are not well-defined, this figure is plausible for the case concerned. While there are several sources of complexity, it may be possible to develop this methodology, both as a technique for fracture toughness measurement (requiring only small samples of simple shape) and as a novel approach to prediction of ballistic impact outcomes.

1. Introduction

The sensitivity of metal plasticity to the rate of deformation is well known, with the flow stress tending to rise significantly when very high strain rates are imposed. The mechanisms responsible for this sensitivity (related to dislocation mobility and alternative deformation modes) are known, but it cannot be predicted in any fundamental way and it is not easy to capture experimentally. Nevertheless, simulation of this strain rate dependence is essential for FEM modelling [1] of many situations involving high strain rates (ballistics, explosions, crashes, machining, cutting etc.). A number of (essentially empirical) constitutive relations have been proposed, with that of Johnson and Cook [2], giving the true (von Mises) stress as a function of the equivalent plastic strain, being frequently used

$$\sigma = \left\{ \sigma_Y + K \epsilon_p^n \right\} \left[1 - \left(\frac{T - T_0}{T_m - T_0} \right)^m \right] \left(1 + C \ln \left\{ \left(\frac{d\epsilon_p}{dt} \right) / \left(\frac{d\epsilon_p}{dt} \right)_0 \right\} \right). \quad (1)$$

where σ_Y is the yield stress, K is the strain hardening coefficient, n is the strain hardening exponent, T_m is the melting temperature, T_0 is a reference (ambient) temperature, m is the temperature coefficient, $(d\epsilon_p/dt)$ is the (plastic) strain rate, $(d\epsilon_p/dt)_0$ is a reference (quasi-static) strain

rate and C is the strain rate sensitivity parameter. Apart from the normalizing strain rate, usually taken to be a quasi-static rate, only the value of C is required in order to characterize the strain rate sensitivity. It should be noted, however, that the temperature dependence is often significant, since the imposition of rapid plastic straining is likely to cause local temperature rises, with most of the plastic work normally being released as heat.

This equation, and variants of it [3–5], are widely used. In general, the basic form is considered to be quite reliable, provided the values of the constants in it can be obtained for the material concerned. This has been done in a variety of ways, including conventional uniaxial testing [6], although this presents severe experimental difficulties at strain rates above about 10^3 s^{-1} (which is the regime in which departure from quasi-static behavior starts to become significant). The split Hopkinson bar (SHB) test [7,8] and the Taylor cylinder test [9–11] are commonly employed, and can create relatively high strain rates ($\sim 10^3$ – 10^5 s^{-1}), although they are subject to a level of uncertainty, arising from various sources [12,13]. Nevertheless, values of C have been obtained many times [14–18] in this way for different metals, ranging in magnitude from about 0.001 to around 0.05. There have also been FEM studies of various test geometries [10,16,17,19], including several covering ballistic impact [20–23], with iterative simulation being used to obtain values of C giving the best fit between experimental and predicted outcomes (such as penetration characteristics, obtained via high speed photography). Such approaches have the capability to predict plastic flow characteristics at very high strain rates with reasonable reliability.

* Corresponding author.

E-mail address: twc10@cam.ac.uk (T. Clyne).

There is, of course, interest, not only in how a metal deforms plastically at high strain rates, but also in how it undergoes failure (fracture). This presents a more severe challenge, since fracture is inevitably a complex process. Several reviews [24–26] cover the issues involved in (FEM) simulation of the fracture of metal samples under impact conditions. This is particularly complex when the sample is in the form of relatively thin plate, for which there have been specific studies on petalling phenomena [27,28], shear plugging failure [29,30] and dishing [31].

Despite these complexities, attempts have been made to identify universal analytical expressions for the prediction of fracture (under high strain rate conditions). For example, Johnson and Cook [32] proposed the following expression for the critical strain, ϵ_f , at which fracture will occur

$$\epsilon_f = [D_1 + D_2 \exp(D_3 \sigma^*)] \left[1 + C \ln \left\{ \left(\frac{d\epsilon_p}{dt} \right) / \left(\frac{d\epsilon_p}{dt} \right)_0 \right\} \right] \times \left[1 + D_4 \left(\frac{T - T_0}{T_m - T_0} \right) \right] \quad (2)$$

where $D_1 - D_4$ are empirical constants. The dependence on the (local) stress state is captured in the first term, in which σ^* is the stress triaxiality (ratio of hydrostatic to deviatoric components). The formulation is plausible in a general sense, since it is common to assume that fracture occurs when a critical level of plastic strain has been reached (ie the ductility of the metal has been “exhausted”), and the general suitability of this is widely accepted [33–39]. Also, a high stress triaxiality often favours fracture (over plasticity) and some sensitivity to temperature and strain rate is also expected (with the sense of these dependences controlled by the signs of the empirical constants). On the other hand, the formulation has no mechanistic basis (in terms of the magnitude of the strain energy release rate for crack propagation or the fracture energy of the material). This also applies to various attempts that have been made [40] to identify a “damage development parameter”, and to correlate this with the equivalent plastic strain.

It should also be mentioned that detailed attempts to assess the reliability of predictions obtained using Eq. (2), and other empirical relationships based on critical strain levels, have sometimes concluded that it is relatively poor. For example, Sharma et al. [41] found that they could not use it to capture the fracture behaviour of an Al alloy being penetrated by hard spheres, although they did claim that there was some correlation with the (tensile) hydrostatic stress level. Dey et al. [42] reported rather similar findings and attempts to use other criteria, such as those of Mohr–Coulomb [43] or Bao–Wierzbicki [44], also encountered limitations.

Of course, the observations on which such comparisons are based are often relatively crude. One of the difficulties is that the kind of fracture being produced during testing has in many cases [45,46] been a “plug” shear failure, in which large amounts of plastic deformation have been produced in the vicinity of the projectile. The final fracture event is often not one of well-defined crack propagation, but simply that of pushing the plug out of the rear face of the sample. In cases such as this, very large plastic strains may be created under conditions such that fracture cannot occur.

What is ideally required is application of the principles of fracture mechanics (ie the energetics associated with fracture events) to experimental situations that create high strain rates (often with high local strain levels), and also well-defined fracture events. An energy-based approach is usually the most fruitful one for fracture, since crack advance must be energetically favourable. However, the energy absorbed (during fracture of a given material) depends on the geometry, which determines the crack propagation mode mix [47–49] and whether the stress field ahead of the crack tip corresponds to plane stress or plane strain (or intermediate) conditions. The fracture energy tends to be quite sensitive to these variations. This is further complicated for ballistic impact by the fact that the stress field varies rapidly with position and time throughout the process. There has in fact been quite longstanding interest in trying to obtain fracture characteristics from crack patterns

around (static) indents, but various severe challenges have been recognized [50–53]. Also, if the interest is in metals then it is in most cases very difficult to induce cracking at quasi-static loading rates, particularly using spherical indenters (and “sharp” indenters introduce uncertainties into both the experiments and the modeling of them).

Nevertheless, there have been at least some fracture mechanics-based investigations of sample failure during impact loading. For example, Xu and Li [54] examined the conditions created during Hopkinson bar testing, using FEM and evaluating the “Dynamic Fracture Toughness” as a function of the crack tip conditions created with different operational parameters (such as striker impact velocity). However, their main conclusion was that this is a very complex area, and that it’s not even clear whether an increase in the imposed strain rate should raise or lower the fracture toughness (or fracture energy). This is in fact plausible, since, while a higher strain rate might be expected to inhibit plastic flow at the crack tip, reducing the toughness, the associated increase in temperature could promote such plasticity, having the opposite effect.

There have also been energy-based (if not fracture mechanics-based) analyses of projectile perforation through thin sheets, one of which [55] highlighted the potential significance of the kinetic energy of ejected fragments. There have also been many studies [56] confirming that the fracture toughness of a material tends to be substantially reduced by high levels of prior plastic strain. Of course, this is well established in a general sense, but such measurements don’t really provide useful information about how fracture is likely to occur in situ during an impact event, which is in most cases a highly dynamic process.

Nevertheless, it should in principle be possible to use an impact test to obtain a value of the fracture energy, from observations of the crack patterns induced under different impact conditions and use of FEM to estimate the strain energy release rate at the point where crack propagation was initiated. The current work is oriented toward that objective. It involves (ballistic) indentation of bulk metallic samples with hard spheres, such that well-defined cracks were created (and captured tomographically). The plasticity characteristics were obtained via iterative FEM, assuming that the Johnson–Cook constitutive relation (Eq. (1)) is obeyed, using a similar approach to that of an earlier paper [23]. A fracture mechanics approach is then used to estimate the strain energy release rate during propagation of observed cracks.

The metal chosen for this work is cast (pure) magnesium. The main reason for this choice is simply that magnesium has a relatively low fracture energy (for a metal), such that well-defined crack propagation can be stimulated by (ballistic) indentation. This characteristic, in combination with reasonably high ductility (capacity for plastic straining) makes it suitable for this study. It should, however, be recognized that Mg does exhibit some complexities, including a tendency for complex twin structures to be generated and for anisotropic behavior to be exhibited. Several studies [57–61] have been undertaken in which the fracture characteristics of Mg alloys have been explored under high strain rate conditions. These characteristics need to be borne in mind when attempting to extract generalized conclusions in this area.

2. Experimental procedures

2.1. Materials and microstructures

A cast (commercial purity) magnesium ingot was used as the source of all of the samples. This was a relatively large ingot, about 150 mm by 75 mm in transverse section and originally about 300 mm long. Both uniaxial compression testing and dynamic (ballistic) indentation with spherical projectiles were carried out. The grain structure of the ingot (transverse section) and the locations of the test samples are shown in Fig. 1. It can be seen that the grain size was coarse (of the order of a few mm, with significant variations). There was also a high incidence of (deformation) twins within the grains, as can be seen in the micrograph

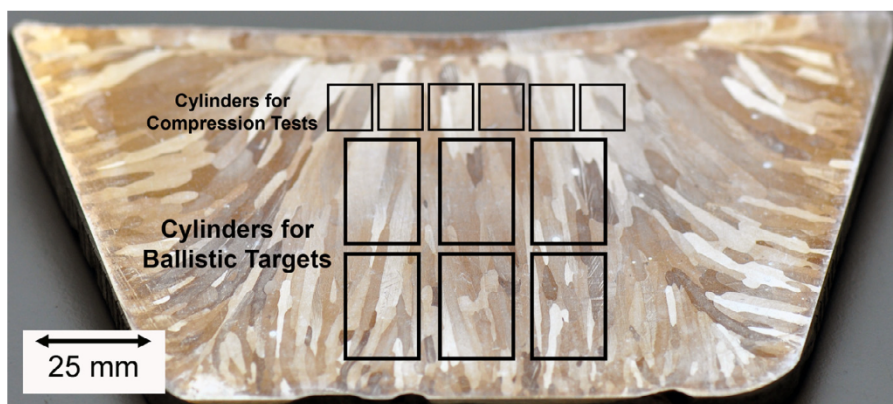


Fig. 1. Photograph of a transverse section of the cast Mg ingot, showing the approximate locations of the cylindrical samples taken from it for compression and ballistic testing.

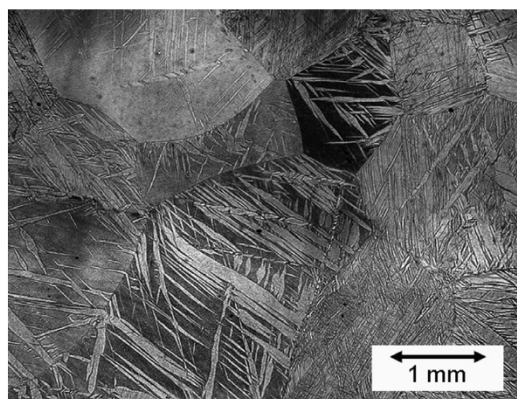


Fig. 2. Optical micrographs of transverse sections of the magnesium from the (a) extruded rod and (b) cast ingot.

shown in Fig. 2. Of course Mg, which has an hexagonal crystal structure, is prone to deformation twinning and these arose just from the stresses created during solidification and cooling of the ingot.

Coarse grain structures such as this present challenges in terms of using indentation to obtain (bulk) properties, since these can only be obtained by mechanically interrogating a representative (multi-grain) volume. The indents were therefore created using relatively large cermet (WC-Co) spheres (of diameter 5 mm), obtained from Bearing Warehouse Ltd (who also supplied a datasheet giving their elastic properties). The resultant indent size depends on both impact velocity and sample hardness, but in general they were of the order of a few mm in diameter, so multi-grain volumes were being tested in all cases. Of course, projectiles in this size range are common, and much smaller ones would have been difficult to use, although (quasi-static) instrumented indentation is often carried out on a finer scale than this.

For present purposes, it is important to be able to simulate the stress-strain curve over a wide range of strain (perhaps up to 200% or more, depending on the depth of projectile penetration). This is well beyond the levels to which conventional uniaxial testing can be carried out (since necking/failure tends to occur in tension and barreling in compression). Extrapolation is therefore necessary.

2.2. Uniaxial compression testing

In order to obtain (quasi-static) plasticity parameter values for this material, samples were subjected to uniaxial compression testing between rigid (hardened steel) platens. Cylindrical specimens (10 mm height, 10 mm diameter) were tested at room temperature ($22^{\circ}\text{C} \pm 2^{\circ}\text{C}$), using MoS_2 lubricant to minimize barreling. Displacements were mea-

sured using an eddy current gage, with a resolution of about $\pm 0.25 \mu\text{m}$. Testing was carried out under displacement control (at a rate of 2 mm min^{-1}), using an Instron 5562 screw-driven testing machine, with a load cell having a capacity of 30 kN. The strain rate generated during these tests, which was taken to be the reference (quasi-static) rate for use in Eq. (1), was thus about $5.5 \cdot 10^{-3} \text{ s}^{-1}$.

Tests were done up to displacements of about 1.5 mm (25% nominal plastic strain), so that each test took about 45 s to complete. It was confirmed that barreling was minimal over this strain range. Tests were carried out over a range of temperature, up to 200°C . (It was confirmed by FEM modeling - see Section 4 - that temperatures reached during ballistic impact were lower than this, except possibly for very short transients in a thin surface layer.)

Several repeat tests were carried out. Both stress and strain levels were converted from nominal to true values, using the standard expressions:

$$\sigma_T = \sigma_N(1 + \epsilon_N), \quad \epsilon_T = \ln(1 + \epsilon_N) \quad (3)$$

with the strains in this case being negative (compressive), so that the true stress has a magnitude lower than the nominal value, while the true strain has a larger magnitude than the nominal strain.

2.3. Ballistic impact experiments

The work is based on the same equipment and procedures as those described in a previous paper [23], so only a very brief description is provided here. The projectiles (5 mm diameter WC-Co cermet balls) were incident on samples that were rigidly supported at the rear, with impact speeds in the range $50\text{--}150 \text{ m s}^{-1}$. The samples were obtained by electrical discharge machining to produce cylinders of diameter 16 mm and height 20 mm, from the locations shown in Fig. 1.

A Phantom V12.1 high-speed camera was used to record impact events, with a time resolution of $\sim 1.4 \mu\text{s}$ (frame rate $\sim 0.72 \text{ MHz}$) and exposure time of $0.285 \mu\text{s}$. From video sequences and known calibration factors, time-displacement histories were extracted for the projectile motion, with attention being focussed on the location of the rear of the projectile.

A Taylor Hobson profilometer (contacting stylus) was used to measure residual indent profiles. Scans were carried out in two perpendicular directions, both through the central axis of the indent (found by carrying out several closely-spaced parallel scans). Tilt correction functions were applied to the raw data, based on the far-field parts of the scan being parallel.

A Bruker Skyscan 1272 X-ray was used in conjunction with the Simpleware Scanip software to reconstruct the subsurface crack structure. The source voltage and source current used were 100 kV and 100 μA , respectively. An Al 1 mm filter, exposure time of 1500 ms and rotation step of 0.15° were used. The resultant resolution was $9 \mu\text{m}$ per pixel.

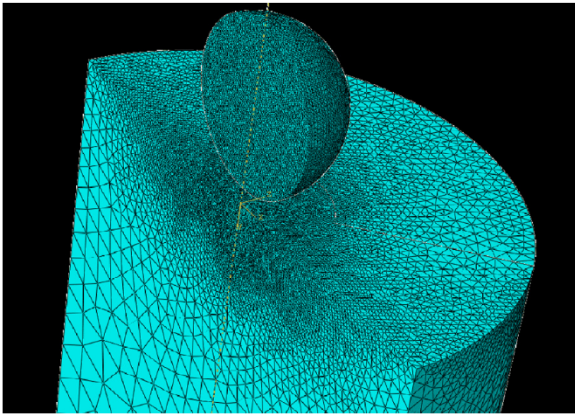


Fig. 3. 3-D visualization of the meshes used for projectile and sample.

2.4. Goodness of fit parameter, g

In order to carry out iterative FEM simulation of the process, the goodness of fit between predicted and experimental outcomes (residual indent profile or displacement-time relationship during impact) must be quantified. There are various ways in which such a parameter can be defined, but in this work the same one is used as in the previous paper [23], where full details are provided. The equation for g (for the case of the outcome being the residual indent profile) may be written

$$g = 1 - \sqrt{\frac{\sum_{i=1}^N \Delta \delta_i^2}{\sum_{i=1}^N (\delta_i - \delta_{av})^2}} \quad (4)$$

The number of radial locations at which the profiles are compared (ie the value of N) can be varied, but would typically be about 100. The value of g can range from 1 (perfect agreement) to zero (no agreement).

3. FEM modelling

3.1. Model formulation and J-C parameter evaluation

The FEM simulation, in terms of meshing, boundary conditions and prediction of the plastic deformation, also conformed closely to the specifications provided in the previous paper [23]. Axi-symmetric meshes were used for both projectile and sample. These are illustrated in Fig. 3. All material properties were assumed to be isotropic. The Young's moduli, E , and Poisson ratios, ν , of projectile and sample were respectively taken to be 650 GPa and 0.21 (cermet) and 45 GPa and 0.29 (Mg). These cermet properties were provided by the supplier (Bearing Warehouse Ltd.). The density of the cermet was measured to be $14,800 \text{ kg m}^{-3}$. The thermal conductivity, κ , of the Mg was taken (from the literature) to be $156 \text{ W m}^{-1} \text{ K}^{-1}$ and its heat capacity, c , to be $1.77 \text{ MJ m}^{-3} \text{ K}^{-1}$. The fraction of the plastic work converted to heat (Taylor-Quinney coefficient) was set at 95%.

Estimation of the J-C parameter (C) was carried out by evaluating the goodness of fit, g (between experimental and predicted indent profiles or displacement-time datasets) and selecting the value of C giving a maximum value of g . Since C is a single parameter, this is a very straightforward operation. (Analogous procedures [62,63] to identify the best fit set of plasticity parameters, such as σ_Y , K and n in Eq. (1), from quasi-static indentation experiments, require more complex searching of parameter space.)

3.2. FEM modelling of crack propagation

In order to simulate the crack propagation event, a cylindrical polar model based on a quadrant was used. Simulation of the impact event

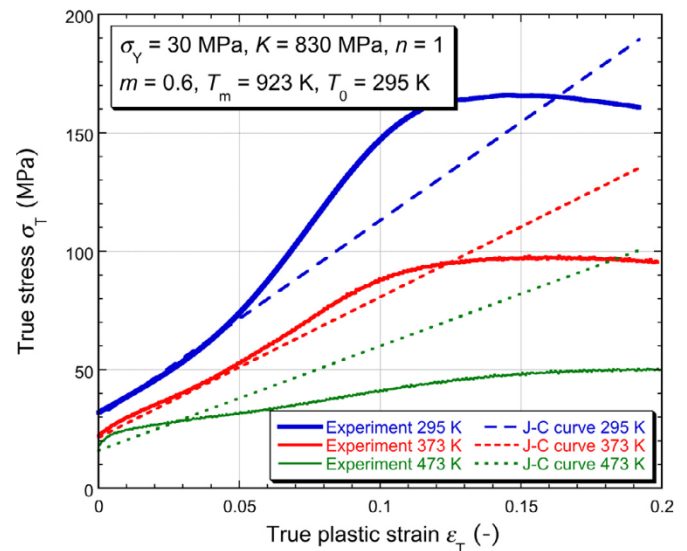


Fig. 4. Experimental stress-strain plots from compression testing over a range of temperature, together with corresponding best fit Johnson-Cook (Eq. (1)) curves, obtained using the parameter set shown.

was halted at the point when the residual energy contained in the projectile had fallen to 20% of its kinetic energy content - the predicted stress fields suggested that this was approximately the stage at which crack initiation took place. Propagation of the crack was modelled by first creating a (cylindrical) interface along which the (circular) crack front would advance. Initially, this interface was fully pinned - i.e. the boundary concerned was a fully cohesive one. The elastic strain energy stored in the system was evaluated. The interface was then unpinned (so that it was free to slide and/or open), up to a selected crack length, and this energy audit was repeated for the new (partially relaxed) stress field. This operation was repeated for further advances of the crack front. For each crack length (and associated crack face area) the strain energy release rate was taken to be the difference between the original and the new levels of stored elastic strain energy, divided by the new crack area created. In order to implement this procedure, while avoiding numerical instability, the time increment was reduced significantly.

It should be clarified at this point that this (pre-defined) cylindrical crack geometry is naturally only a crude reflection of the observed behavior. The cracks certainly did not form as perfect cylinders. In fact, it would be difficult to establish exactly what crack path would be favoured, even for an isotropic, homogeneous continuum, and the (anisotropic, inhomogeneous) microstructure adds a further complication. Nevertheless, this crack geometry can be taken as broadly representative of the behavior of the system.

4. Effects of temperature and strain rate on plasticity

4.1. Quasi-static stress-strain plots as a function of temperature

Stress-strain curves are shown in Fig. 4 for three different temperatures, after elimination of the elastic component and conversion to true values (using Eq. (3)). It should first be noted that the reduction in true stress as the strain rises above about 12%, observed for the two lower temperatures, is probably not a real effect. It is certainly not expected, provided the stress and strain fields remain uniform (throughout the gauge length). In fact, in this particular case, it was probably due to (observed) inter-granular cracking at the free surface, leading in some cases to actual loss of grains from the sample (as a result of the creation of intersecting near-surface crack patterns). This kind of behavior is not uncommon with Mg alloys [60,61]. In view of this, the real plasticity characteristics exhibited by this material (as a function of temperature)

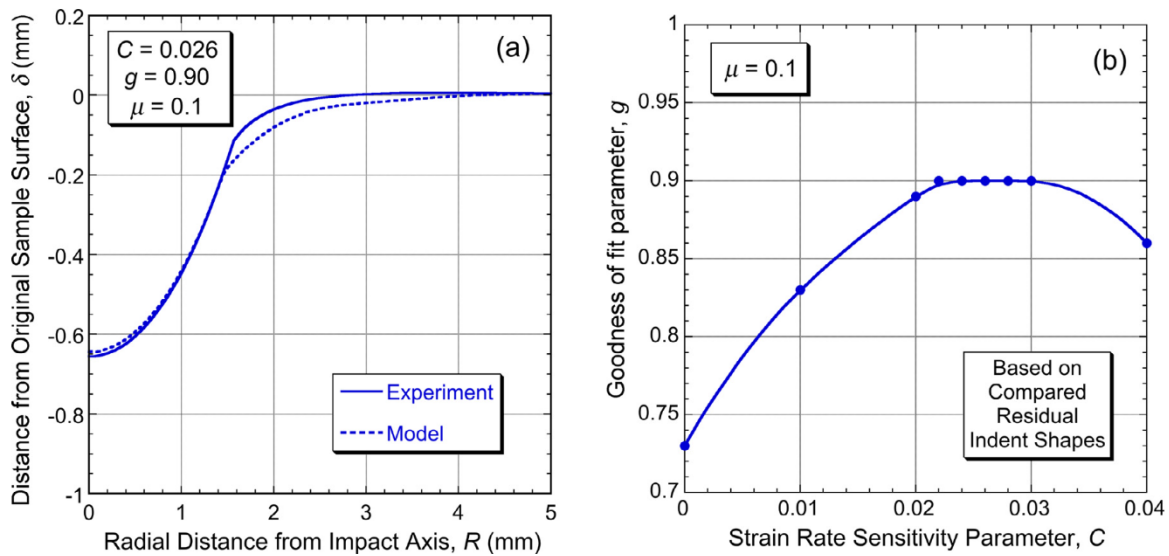


Fig. 5. Residual indent shape data for an impact velocity of 50 m s^{-1} , showing (a) a comparison between experiment and FEM prediction, for the best fit value of C , and (b) the dependence of the goodness of fit parameter on the value of C used in the model.

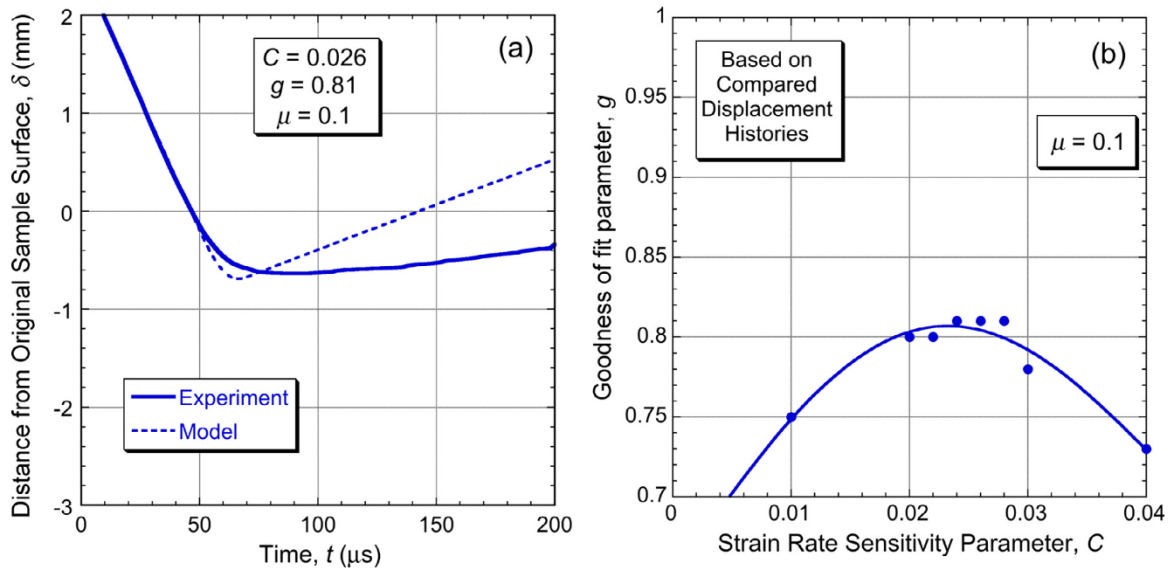


Fig. 6. Displacement-time data during projectile impact and rebound, for an impact velocity of 50 m s^{-1} , showing (a) a comparison between experiment and FEM prediction, for the best fit value of C , and (b) the dependence of the goodness of fit parameter on the value of C used in the model.

are probably captured at least semi-quantitatively by Eq. (1), using the set of parameter values shown in the plot. Of course, it should be recognized that there are significant limitations to this procedure, one of which is that this material is probably quite strongly textured (and hence plastically anisotropic). Mg is certainly known to exhibit relatively complex stress-strain characteristics, partly as a result of high levels of twinning. It may also be noted that these plots reflect the response when loaded parallel to the axis of the columnar zone (Fig. 1), whereas (ballistic) indentation generates multi-directional deformation.

4.2. Effect of strain rate and evaluation of C

A magnitude of C for this material was estimated by repeatedly running the FEM model, using Eq. (1) to represent the plasticity. The value of C in this expression was progressively varied, while the values of the other parameters in it were held at those shown in Fig. 4 and the reference (quasi-static) strain rate was taken as the one used in the

compression tests (Section 2.2). Fig. 5 shows, for an impact velocity of 50 m s^{-1} , (a) a comparison between measured and modeled residual indent shapes, for the best fit value of C , and (b) the dependence of the goodness of fit parameter, g , on the value of C used in the model. This (low) velocity was chosen because it created no cracks, since these do influence the response of the sample. It can be seen that the best fit value for C is about 0.026, although it should be noted that the fit is not perfect (g is not very close to 1) and the peak is not a sharp one. Nevertheless, a value in the range 0.02–0.03 seems appropriate and this should be sufficiently accurate to at least approximately capture the plastic deformation under these impact conditions. This is confirmed by Fig. 6, which shows the corresponding comparisons for the displacement-time data obtained via high speed photography. While there is no reported value of C in the literature for anything resembling this material, it is certainly in the expected range [6,14–18,23], particularly since relatively soft metals like this, with potential for work hardening, tend to exhibit relatively high values.

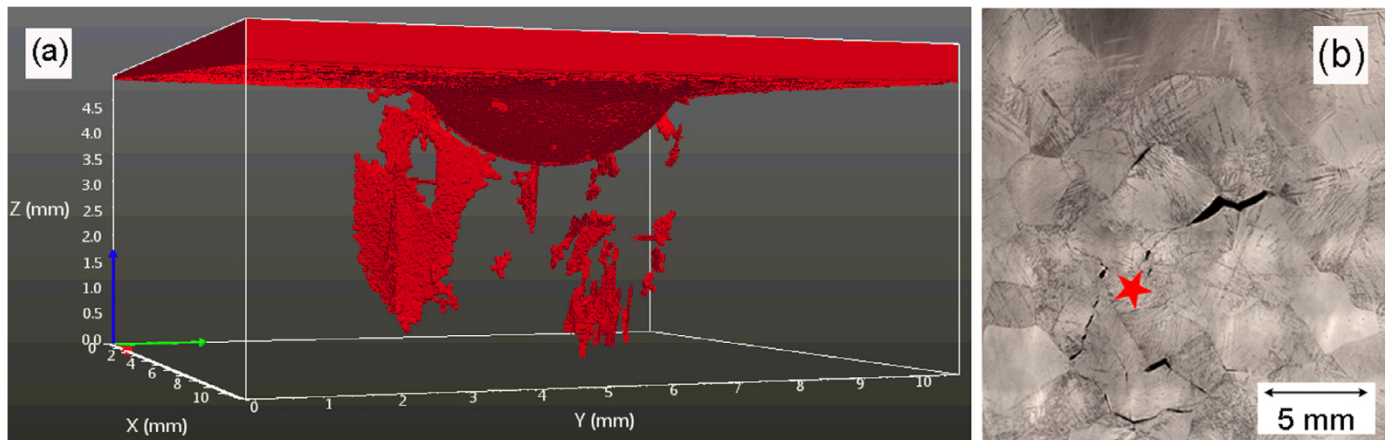


Fig. 7. Crack patterns after impact with a velocity of 120 m s^{-1} , illustrated by (a) a tomographic visualization and (b) a metallographic section normal to the axis of the projectile motion (marked with a star), at a depth of 2.8 mm below the original free surface.

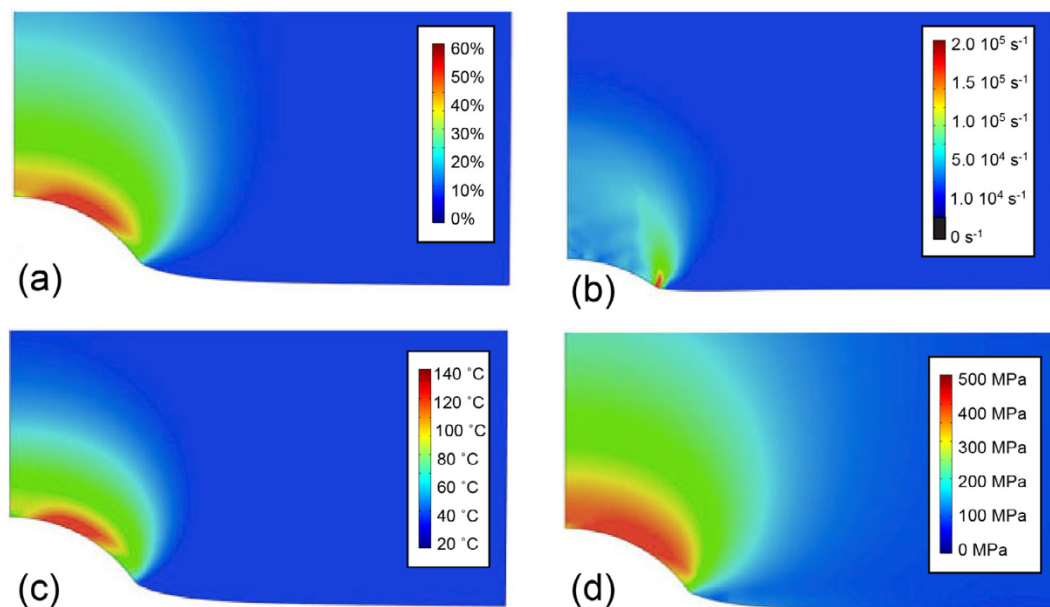


Fig. 8. Fields of (a) plastic strain, (b) strain rate, (c) temperature and (d) von Mises stress, for an incident velocity of 120 m s^{-1} , each field being shown at the stage when the peak value was attained. (An indication of the stages concerned can be obtained from the penetration depths.)

5. Evaluation of the fracture energy

5.1. Tomographic capture of crack patterns

Well-defined cracking – mostly inter-granular – was observed with the higher impact velocities ($> \sim 100 \text{ m s}^{-1}$) used in this work. In order to analyse their initiation and growth, their location and orientation are required. It was found that they provided good contrast in tomographic images. A representative example can be seen Fig. 7, which also shows a polished section from the same sample. The latter confirms that the cracking is predominantly inter-granular, and also shows that some of these cracks opened up significantly, suggesting that they formed with a strong mode I (“crack opening mode”) component. This is also consistent with the strong contrast seen in tomographic images. Of course, the crack pattern is somewhat irregular, and this was true of most such images. It does not, for example, exhibit clear radial symmetry. This is unsurprising in view of the tendency towards inter-granular cracking and the coarse, rather irregular grain structure. Nevertheless, tomographic images like this did give indications of the nature and orientation of the cracking, and an idea of typical crack lengths (from the free

surface). Cracks mainly propagated in a direction normal to the original free surface, with the crack plane showing a tendency to lie in the “hoop” plane (normal to the radial direction). They could thus be described as “Hertzian”, although with a shape that is closer to a cylinder than a cone. They mostly appear to originate around the periphery of the “impact crater”.

5.2. Stress, strain, strain rate and temperature fields

The FEM model can be used to provide insights into the conditions under which crack initiation and propagation occurred. An example is provided by Fig. 8, which shows the fields concerned at the stages when peak values were obtained, for an incident velocity of 120 m s^{-1} . These give a general feel for the conditions that were created during impact (strains of up to $\sim 60\%$, strain rates up to $\sim 10^5 \text{ s}^{-1}$, temperatures up to $\sim 140^\circ\text{C}$ and deviatoric stresses up to $\sim 500 \text{ MPa}$). However, this type of information doesn’t really provide any pointers towards the onset of cracking. For example, using a “critical strain” criterion would suggest that cracking should start deep within the indent, rather than around the rim of the impact crater where they are actually observed. What

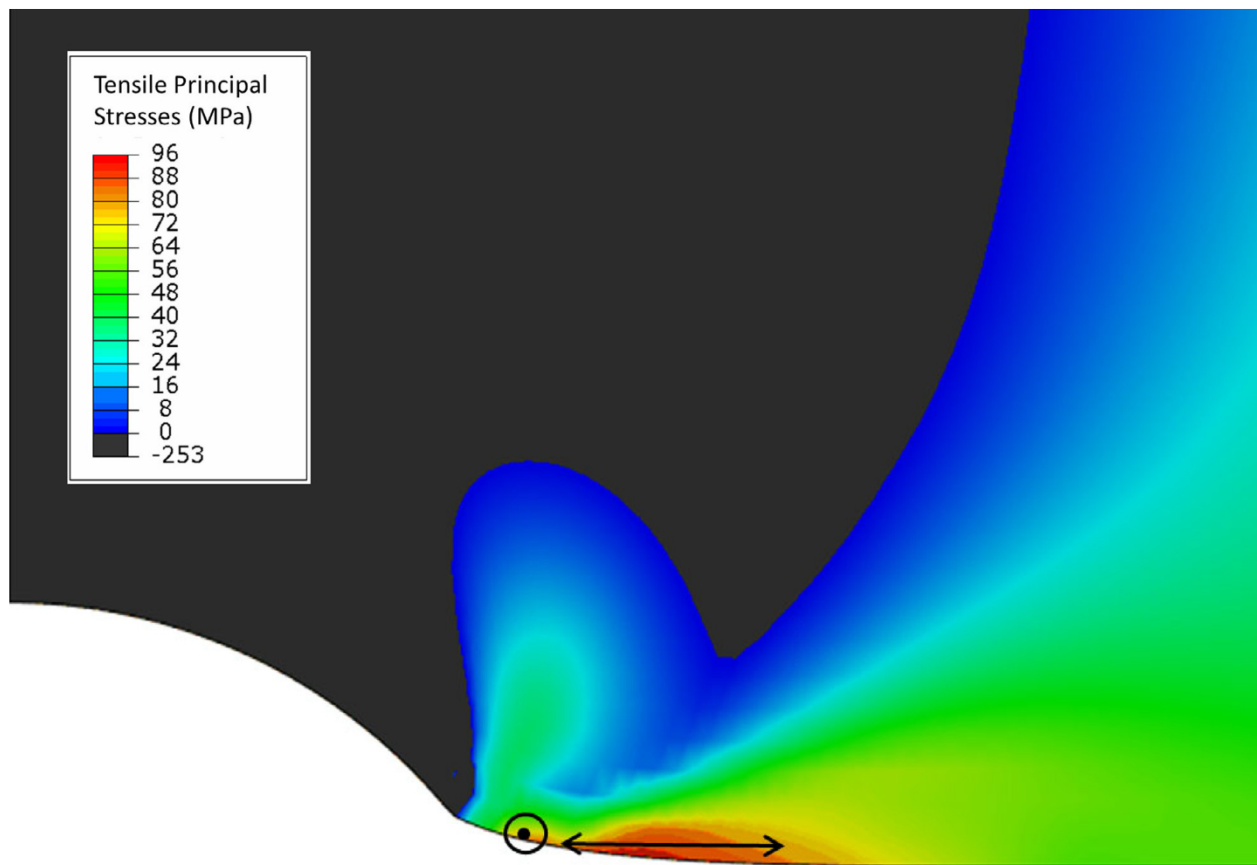


Fig. 9. Field showing the location of the largest tensile principal stress (with directions indicated in two locations), for an impact velocity of 120 m s^{-1} . This occurred $9 \mu\text{s}$ after initial contact (1.05 mm penetration).

is needed here is more detailed consideration of the stress field (and strain energy release rates that would be associated with cracking in a particular configuration).

5.3. Simulation of crack growth

Since the observed cracks appear to have grown under predominantly mode I loading, attention should be focused on the tensile stresses generated during impact. Fig. 9 shows contours of the largest tensile principal stresses created during the process (with an impact velocity of 120 m s^{-1}). It can be seen that these did occur in the vicinity of the rim of the impact crater. This suggests that (mode I) cracks are expected to initiate first in that location, under the influence of the tensile stress (of $\sim 100 \text{ MPa}$) indicated by the arrow. This is encouraging in the sense that the observed cracking can be reconciled with the predicted stress field (but not with the application of any type of critical strain criterion). However, the value of 100 MPa is probably not of any significance and indeed attempts to identify “fracture strengths” of materials, expressed as a stress level, are in general unsuccessful, particularly for metals.

The real objective is to estimate the fracture energy, recognizing the conditions under which crack propagation occurred. (In this case, approximately plane strain conditions applied and the mode mix was predominantly mode I.) The fracture energy was obtained by simulation of crack advance, assumed to occur without further projectile motion, as outlined in Section 3.2. The crack plane was predetermined - in this case a cylinder with radius equal to the distance from the axis to the location of peak tensile stress. This plane was initially pinned, with the stress field concerned. The crack front was then allowed to advance (ie the plane was unpinned) by a series of increments - see Fig. 10 driven by

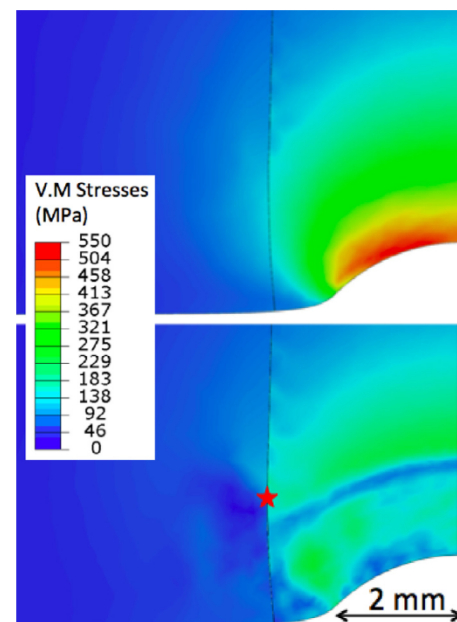


Fig. 10. Von Mises stress fields before and after crack advance (from the free surface to the marked location).

the stress relaxation (and associated release of strain energy) that this allowed.

After each advance, the stored elastic strain energy was audited and the strain energy release rate taken as the reduction in energy divided

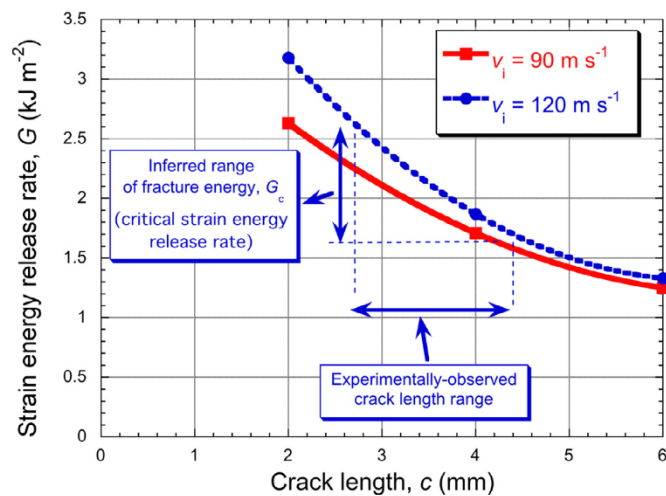


Fig. 11. Strain energy release rates during crack advance, due to the stress fields arising during impact, and inferred fracture energy range.

by the increase in crack area. The outcome is shown in Fig. 11, for two impact velocities and for three different crack lengths. An indication of the fracture energy (critical strain energy release rate) can be obtained from observed crack lengths. Of course, these are not well-defined, but in general they were observed to be of the order of 3–4 mm for both of these impact velocities - see Fig. 7(a) for an indication of this - and, as shown in Fig. 11, this leads to an estimate of the fracture energy having a magnitude of the order of 2 kJ m^{-2} . With this particular material, it wasn't possible to carry out a conventional fracture toughness measurement, and in any event part of the argument here is that the effective toughness is likely to be different (lower) under impact conditions, when (crack tip) plasticity is inhibited. Nevertheless, it may be noted that this fracture energy value, which is relatively low (for a metal), actually appears to be quite plausible, recognizing that Mg is less tough than most metals.

It must be recognized that the work presented here incorporates a number of fairly severe simplifications and approximations, both in terms of the details of the modeling and concerning experimental data and observations. This is partly a reflection of the difficulty of creating well-defined crack patterns under high strain rate loading. However, it also relates to the severe challenges faced when attempting to model dynamic crack propagation under impact conditions, using a rigorous fracture mechanics approach. It is certainly a much more complex undertaking than that of using the "conventional" approach of simply defining a critical strain, at which fracture is expected to occur. Nevertheless, since the latter undoubtedly has serious limitations, it may be considered worthwhile to attempt to take the fracture mechanics approach a little further than the very rudimentary study presented here. It's certainly likely that substantial improvements can quite readily be made in the modeling methodology.

6. Conclusions

Ballistic impact experiments have been carried out, using hard spheres as the projectile and thick samples machined from a cast Mg ingot as the target. This material was chosen in view of its relatively low toughness (compared with many metals). With impact velocities of at least about 100 m s^{-1} , networks of cracks were created. Their geometry was captured using X-ray tomography. They were broadly of a Hertzian type, although approximately cylindrical, rather than conical, and were mostly initiated close to the rim of the impact crater.

FEM simulation was carried out, with the dependence on strain rate of the plasticity being captured via the Johnson–Cook formulation, using an experimentally-determined value of the strain rate sensitivity param-

eter. The focus was on attempting to understand and predict observed features of the crack initiation and propagation. It was noted that, during impact, relatively high tensile stresses were created around the rim of the impact crater, oriented in the radial direction. It is likely that these stimulated initiation of many of the observed cracks.

A novel procedure is proposed for evaluation of the fracture energy of the material, based on such observed crack patterns. This involves using the FEM model to predict the stress field, and hence the stored elastic strain energy in the sample, before and after allowing the crack to propagate by the observed distance (a few mm in these cases). This was done by "unpinning" an interface (designed to represent the crack plane), up to a series of specified crack lengths. This interface was a cylinder with a radius corresponding to the position around the rim where cracking was observed to initiate. This procedure led to an estimated value for the critical strain energy release rate (fracture energy) of $\sim 2 \text{ kJ m}^{-2}$. There is no alternative way of measuring this property under corresponding conditions (since it is likely to be affected by the very high crack propagation rate), but it is approximately in the range that might have been expected.

Declaration of Competing Interests

The authors declare that they have no known competing financial interests or personal relationships that could have appeared to influence the work reported in this paper.

Acknowledgements

This work has been supported by EPSRC (grant EP/I03869/1) and also by AWE (contract Ref. No. 30356290), as part of an ongoing collaboration aimed at the development of robust and user-friendly tools for the extraction of mechanical property characteristics from instrumented indentation data. The authors are particularly grateful to Dr. Giles Aldrich-Smith and Dr. Nigel Park, of AWE, for extensive discussions and interactions. Funding has also been received from the Leverhulme Trust (ref IN-2016-004), via a grant supporting an International Network, and from Downing College (via the Thrower fund).

In compliance with current EPSRC requirements, input data for the modeling described in this paper, including meshing and boundary condition specifications, are available at the following URL: www.ccg.msm.cam.ac.uk/publications/resources. These files can be downloaded and used in FEM models.

Supplementary materials

Supplementary material associated with this article can be found, in the online version, at doi:10.1016/j.mta.2020.100652.

References

- [1] D. Umbrello, R. M'Saoubi, J.C. Outeiro, The influence of Johnson–Cook material constants on finite element simulation of machining of AISI 316L steel, *Int. J. Mach. Tools Manuf.* 47 (3–4) (2007) 462–470.
- [2] G.R. Johnson, W.H. Cook, A constitutive model and data for metals subjected to large strains, high strain rates and high temperatures, in: *Proceedings of the 7th International Symposium on Ballistics*, 21, 1983, pp. 541–547.
- [3] W.K. Rule, S.E. Jones, A revised form for the Johnson–Cook strength model, *Int. J. Impact Eng.* 21 (8) (1998) 609–624.
- [4] Y.C. Lin, X.M. Chen, G. Liu, A modified Johnson–Cook model for tensile behaviors of typical high-strength alloy steel, *Mater. Sci. Eng. Struct. Mater. Prop. Microstruct. Proc.* 527 (26) (2010) 6980–6986.
- [5] A. He, G.L. Xie, H.L. Zhang, X.T. Wang, A comparative study on Johnson–Cook, modified Johnson–Cook and arrhenius-type constitutive models to predict the high temperature flow stress in 20Crmo alloy steel, *Mater. Des.* 52 (2013) 677–685.
- [6] J.L. Jordan, C.R. Siviour, G. Sunny, C. Bramlette, J.E. Spowart, Strain rate-dependant mechanical properties of OFHC copper, *J. Mater. Sci.* 48 (20) (2013) 7134–7141.
- [7] L.D. Bertholf, C.H. Karnes, 2-dimensional analysis of split Hopkinson pressure bar system, *J. Mech. Phys. Solids* 23 (1) (1975) 1–19.
- [8] W.N.W. Chen, B. Song, *Split Hopkinson (Kolsky) Bar: Design, Testing and Applications*. Split Hopkinson, Springer, New York, 2011.

- [9] P.J. Maudlin, J.F. Bingert, J.W. House, S.R. Chen, On the modeling of the Taylor cylinder impact test for orthotropic textured materials: experiments and simulations, *Int. J. Plast.* 15 (2) (1999) 139–166.
- [10] P.J. Maudlin, G.T. Gray, C.M. Cady, G.C. Kaschner, High-Rate material modeling and validation using the Taylor cylinder impact test, *Philos. Trans. R. Soc. Math. Phys. Eng. Sci.* 357 (1756) (1999) 1707–1729.
- [11] S.L. Lopatnikov, B.A. Gama, M.J. Haque, C. Krauthauser, J.W. Gillespie, M. Guden, I.W. Hall, Dynamics of metal foam deformation during Taylor cylinder-Hopkinson bar impact experiment, *Compos. Struct.* 61 (1–2) (2003) 61–71.
- [12] B.A. Gama, S.L. Lopatnikov, J.W. Gillespie Jr, Hopkinson bar experimental technique: a critical review, *Appl. Mech. Rev.* 57 (2004) 223.
- [13] D.A. Prabowo, M.A. Kariem, L. Gunawan, in: N.K. Gupta, M.A. Iqbal (Eds.), The effect of specimen dimension on the results of the split-Hopkinson tension bar testing, Elsevier Science Bv, Amsterdam, 2017, pp. 608–614.
- [14] H.G. Noh, W.J. An, H.G. Park, B.S. Kang, J. Kim, Verification of dynamic flow stress obtained using split Hopkinson pressure test bar with high-speed forming process, *Int. J. Adv. Manuf. Technol.* 91 (1–4) (2017) 629–640.
- [15] G.I. Mylonas, G.N. Labeas, Mechanical characterization of aluminium alloy 7449-T7651 at high strain rates and elevated temperatures using split Hopkinson bar testing, *Exp. Tech.* 38 (2) (2014) 26–34.
- [16] M. Sedighi, M. Khandaei, H. Shokrollahi, An approach in parametric identification of high strain rate constitutive model using Hopkinson pressure bar test results, *Mater. Sci. Eng. Struct. Mater. Prop. Microstruct. Proces.* 527 (15) (2010) 3521–3528.
- [17] M. Sasso, G. Newaz, D. Amodio, Material characterization at high strain rate by Hopkinson bar tests and finite element optimization, *Mater. Sci. Eng. Struct. Mater. Prop. Microstruct. Proces.* 487 (1–2) (2008) 289–300.
- [18] A. Mishra, M. Martin, N.N. Thadhani, B.K. Kad, E.A. Kenik, M.A. Meyers, High-Strain-Rate response of ultra-fine-grained copper, *Acta Mater.* 56 (12) (2008) 2770–2783.
- [19] A. Gavrus, J.P. Le Baron, P. Caestecker, E. Ragneau, Investigation of high speed behaviour of ductile materials by computer simulation and Hopkinson experimental test, in: D. Miannay, P. Costa, D. Francois, A. Pineau (Eds.), Proceedings of the Advances in Mechanical Behaviour, Plasticity and Damage, 1 and 2, Elsevier Science Bv, Amsterdam, 2000, pp. 535–540.
- [20] E. Andrews, A.E. Giannakopoulos, E. Plisson, S. Suresh, Analysis of the impact of a sharp indenter, *Int. J. Solids Struct.* 39 (2002) 281–295.
- [21] J. Lu, S. Suresh, G. Ravichandran, Dynamic indentation for determining the strain rate sensitivity of metals, *J. Mech. Phys. Solids* 51 (2003) 1923–1938.
- [22] G. Skordaris, K.D. Bouzakis, P. Charalampous, A dynamic fem simulation of the nano-impact test on mono- or multi-layered PVD coatings considering their graded strength properties determined by experimental-analytical procedures, *Surf. Coat. Technol.* 265 (2015) 53–61.
- [23] M. Burley, J.E. Campbell, J. Dean, T.W. Clyne, Johnson–Cook parameter evaluation from ballistic impact data via iterative fem modeling, *Int. J. Impact Eng.* 112 (2018) 180–192.
- [24] R.S.J. Corran, P.J. Shadbolt, C. Ruiz, Impact loading of plates - an experimental investigation, *Int. J. Impact Eng.* 1 (1) (1983) 3–22.
- [25] C.E. Anderson, S.R. Bodner, Ballistic impact: the status of analytical and numerical modelling, *Int. J. Impact Eng.* 7 (1) (1988) 9–35.
- [26] G.G. Corbett, S.R. Reid, W. Johnson, Impact loading of plates and shells by free flying projectiles, *Int. J. Impact Eng.* 18 (2) (1996) 141–230.
- [27] T. Wierzbicki, Petalling of plates under explosive and impact loading, *Int. J. Impact Eng.* 22 (1999) 935–954.
- [28] B. Landkof, W. Goldsmith, Petalling of thin metallic plates during penetration by cylindrical-conical projectiles, *Int. J. Solids Struct.* 21 (3) (1983) 245–266.
- [29] A.G. Atkins, M.A. Khan, J.H. Liu, Necking and radial cracking around perforations in thin sheets at normal incidence, *Int. J. Impact Eng.* 21 (7) (1998) 521–539.
- [30] T. Borvik, O.S. Hopperstad, T. Berstad, M. Langseth, Numerical simulation of plugging failure in ballistic penetration, *Int. J. Solids Struct.* 38 (1999) 6241–6264.
- [31] Y.W. Lee, T. Wierzbicki, Fracture prediction of thin plates under localised impulsive loading. Part 1: dishing, *Int. J. Impact Eng.* 31 (2005) 1253–1276.
- [32] G.R. Johnson, W.H. Cook, Fracture characteristics of 3 metals subjected to various strains, strain rates, temperatures and pressures, *Eng. Fract. Mech.* 21 (1) (1985) 31–48.
- [33] N.K. Gupta, M.A. Iqbal, G.S. Sekhon, Experimental and numerical studies on the behaviour of thin aluminium plates subjected to impact by blunt- and hemispherical-nosed projectiles, *Int. J. Impact Eng.* 32 (2006) 1921–1944.
- [34] T. Borvik, H.A. Clausen, M. Eriksson, T. Berstad, O.S. Hopperstad, M. Langseth, Experimental and numerical study on the perforation of Aa6005-T6 panels, *Int. J. Impact Eng.* 32 (2005) 35–64.
- [35] T. Borvik, M. Langseth, O.S. Hopperstad, A.K. Malo, Ballistic penetration of steel plates, *Int. J. Impact Eng.* 22 (1999) 855–886.
- [36] T. Borvik, O.S. Hopperstad, T. Berstad, M. Langseth, Perforation of 12 mm thick steel plates by 20 mm diameter projectiles with flat, hemispherical and conical noses part 2: numerical simulations, *Int. J. Impact Eng.* 27 (2002) 37–64.
- [37] X. Teng, T. Wierzbicki, Evaluation of six fracture models in high velocity perforation, *Eng. Fract. Mech.* 73 (2006) 1653–1678.
- [38] W.S. Lee, C.F. Lin, T.J. Liu, Impact and fracture response of sintered 316L stainless steel subjected to high strain rate loading, *Mater. Charact.* 58 (4) (2007) 363–370.
- [39] H.R. Wang, C.Y. Cai, D.N. Chen, D.F. Ma, Dynamic constitutive behavior and fracture of lanthanum metal subjected to impact compression at different temperatures and impact tension, *Int. J. Nonlinear Sci. Numer. Simul.* 14 (1) (2013) 15–26.
- [40] S.S. Gautam, R. Babu, P.M. Dixit, Ductile fracture simulation in the Taylor rod impact test using continuum damage mechanics, *Int. J. Damage Mech.* 20 (3) (2011) 347–369.
- [41] P. Sharma, P. Chandel, P. Mahajan, M. Singh, Quasi-Brittle fracture of aluminium alloy 2014 under ballistic impact, in: N.K. Gupta, M.A. Iqbal (Eds.), Proceedings of the Plasticity and Impact Mechanics, Elsevier Science Bv, Amsterdam, 2017, pp. 206–213.
- [42] S. Dey, T. Borvik, O.S. Hopperstad, M. Langseth, On the influence of fracture criterion in projectile impact of steel plates, *Comput. Mater. Sci.* 38 (1) (2006) 176–191.
- [43] X.K. Xiao, H. Pan, Y.L. Bai, Y.S. Lou, C. Lin, Application of the modified Mohr–Coulomb fracture criterion in predicting the ballistic resistance of 2024-T351 aluminum alloy plates impacted by blunt projectiles, *Int. J. Impact Eng.* 123 (2019) 26–37.
- [44] A. Gilioli, A. Manes, M. Giglio, T. Wierzbicki, Predicting ballistic impact failure of aluminium 6061-T6 with the rate-independent Bao-Wierzbicki fracture model, *Int. J. Impact Eng.* 76 (2015) 207–220.
- [45] F. Martinez, L.E. Murr, A. Ramirez, M.I. Lopez, S.M. Gaytan, Dynamic deformation and adiabatic shear microstructures associated with ballistic plug formation and fracture in Ti-6Al-4V targets, *Mater. Sci. Eng. Struct. Mater. Prop. Microstruct. Proces.* 454 (2007) 581–589.
- [46] H. Rojacz, M. Hutterer, H. Winkelmann, High temperature single impact studies on material deformation and fracture behaviour of metal matrix composites and steels, *Mater. Sci. Eng. Struct. Mater. Prop. Microstruct. Proces.* 562 (2013) 39–45.
- [47] R.J. Nuismer, Energy release rate criterion for mixed mode fracture, *Int. J. Fract.* 11 (2) (1975) 245–250.
- [48] A. Seweryn, A non-local stress and strain energy release rate mixed mode fracture initiation and propagation criteria, *Eng. Fract. Mech.* 59 (6) (1998) 737–760.
- [49] F. Berto, M.R. Ayatollahi, T. Borsato, P. Ferro, Local strain energy density to predict size-dependent brittle fracture of cracked specimens under mixed mode loading, *Theor. Appl. Fract. Mech.* 86 (2016) 217–224.
- [50] J. den Toonder, J. Malzbender, G. de With, R. Balkenende, Fracture toughness and adhesion energy of sol-gel coatings on glass, *J. Mater. Res.* 17 (1) (2002) 224–233.
- [51] G.D. Quinn, R.C. Bradt, On the vickers indentation fracture toughness test, *J. Am. Ceram. Soc.* 90 (3) (2007) 673–680.
- [52] J. Chen, On the determination of coating toughness during nanoindentation, *Surf. Coat. Technol.* 206 (13) (2012) 3064–3068.
- [53] K. Wasmer, C. Pouvreau, J.M. Breguet, J. Michler, D. Schulz, J.H. Giovanola, Nanoindentation cracking in gallium arsenide: part I in situ sem nanoindentation, *J. Mater. Res.* 28 (20) (2013) 2785–2798.
- [54] Z.J. Xu, Y.L. Li, Dynamic fracture toughness of high strength metals under impact loading: increase or decrease, *Acta Mechanica Sinica* 27 (4) (2011) 559–566.
- [55] J. Dean, C.S. Dunleavy, P.M. Brown, T.W. Clyne, Energy absorption during projectile perforation of thin steel plates and the kinetic energy of ejected fragments, *Int. J. Impact Eng.* 36 (10–11) (2009) 1250–1258.
- [56] K.T. Schwarz, K.S. Kormout, R. Pippa, A. Hohenwarther, Impact of severe plastic deformation on microstructure and fracture toughness evolution of a duplex-steel, *Mater. Sci. Eng. Struct. Mater. Prop. Microstruct. Proces.* 703 (2017) 173–179.
- [57] G.V. Garkushin, G.I. Kanel, S.V. Razorenov, High strain rate deformation and fracture of the magnesium alloy Ma2-1 under shock wave loading, *Phys. Solid State* 54 (5) (2012) 1079–1085.
- [58] M.A.M. Daud, N.Z. Nasir, A. Rivai, M.Z. Selamat, Dynamic fracture toughness of magnesium alloy under impact loading conditions, in: S.A. Aljunid, M.S. Anuar, M.N. Salimi, K.A. Ismail (Eds.), Proceedings of the Malaysian Technical Universities Conference on Engineering & Technology 2012, Elsevier Science Bv, Amsterdam, 2013, pp. 639–644.
- [59] L. Zhou, Y.F. Guo, Dislocation-governed plastic deformation and fracture toughness of nanotwinned magnesium, *Materials (Basel)* 8 (8) (2015) 5250–5264.
- [60] A. Malik, Y.W. Wang, H.W. Cheng, M.A. Khan, F. Nazeer, R. An, J.W. Bao, M.J. Wang, Fracture behavior of twin induced ultra-fine grained Zk61 magnesium alloy under high strain rate compression, *J. Mater. Res. Technol. JMR&T* 8 (4) (2019) 3475–3486.
- [61] W.T. Jia, L.F. Ma, Q.C. Le, C.C. Zhi, P.T. Liu, Deformation and fracture behaviors of AZ31B Mg alloy at elevated temperature under uniaxial compression, *J. Alloys Compd.* 783 (2019) 863–876.
- [62] J.E. Campbell, R.P. Thompson, J. Dean, T.W. Clyne, Comparison between stress-strain plots obtained from indentation plastometry, based on residual indent profiles, and from uniaxial testing, *Acta Mater.* 168 (2019) 87–99.
- [63] J.E. Campbell, R.P. Thompson, J. Dean, T.W. Clyne, Experimental and computational issues for automated extraction of plasticity parameters from spherical indentation, *Mech. Mater.* 124 (2018) 118–131.